



HAL
open science

Structure and luminescent properties of Dy³⁺ activated NaLa₉(SiO₄)₆O₂ yellow-emitting phosphors for application in white LEDs

Sami Slimi, Pavel Loiko, Kirill Bogdanov, Anna Volokitina, Rosa Maria Solé, Magdalena Aguiló, Francesc Díaz, Ezzedine Ben Salem, Xavier Mateos

► To cite this version:

Sami Slimi, Pavel Loiko, Kirill Bogdanov, Anna Volokitina, Rosa Maria Solé, et al.. Structure and luminescent properties of Dy³⁺ activated NaLa₉(SiO₄)₆O₂ yellow-emitting phosphors for application in white LEDs. *Journal of Alloys and Compounds*, 2022, 896, pp.163109. 10.1016/j.jallcom.2021.163109 . hal-03858690

HAL Id: hal-03858690

<https://hal.science/hal-03858690>

Submitted on 17 Nov 2022

HAL is a multi-disciplinary open access archive for the deposit and dissemination of scientific research documents, whether they are published or not. The documents may come from teaching and research institutions in France or abroad, or from public or private research centers.

L'archive ouverte pluridisciplinaire **HAL**, est destinée au dépôt et à la diffusion de documents scientifiques de niveau recherche, publiés ou non, émanant des établissements d'enseignement et de recherche français ou étrangers, des laboratoires publics ou privés.



Distributed under a Creative Commons Attribution 4.0 International License

Structure and luminescent properties of Dy³⁺ activated NaLa₉(SiO₄)₆O₂ yellow-emitting phosphors for application in white LEDs

Sami Slimi^{1,2}, Pavel Loiko³, Kirill Bogdanov⁴, Anna Volokitina^{1,4}, Rosa Maria Solé¹, Magdalena Aguiló¹, Francesc Díaz¹, Ezzedine Ben Salem², and Xavier Mateos^{1,#,*}

¹*Universitat Rovira i Virgili (URV), Física i Cristal·lografia de Materials i Nanomaterials (FiCMA-FiCNA), Marcel·li Domingo 1, 43007 Tarragona, Spain*

²*I.P.E.I. of Monastir, Unit of Materials and Organic Synthesis, 5019 Monastir, UR17ES31, Tunisia*

³*Centre de Recherche sur les Ions, les Matériaux et la Photonique (CIMAP), UMR 6252 CEA-CNRS-ENSICAEN, Université de Caen Normandie, 6 Boulevard du Maréchal Juin, 14050 Caen Cedex 4, France*

⁴*ITMO University, 49 Kronverkskiy Pr., 197101 St. Petersburg, Russia*

[#]*Serra Hünter Fellow*

^{*}*Corresponding author, e-mail: xavier.mateos@urv.cat*

ABSTRACT: A series of NaLa_{9-x}Dy_x(SiO₄)₆O₂ (NLSO:xDy, x = 0 – 0.3) apatite phosphors were synthesized by solid-state reaction at 1100 °C. Their crystal structure, morphology and particle size distribution, electronic structure, Raman spectra, as well as concentration- and temperature-dependent luminescent properties were investigated for the first time. The crystal structure is refined by the Rietveld method. Undoped NLSO is hexagonal (space group $P6_3/m - C_{2h}^{26}$) with lattice constants $a = b = 9.6917(3)$ Å and $c = 7.1836(4)$ Å. Dy³⁺ ions substitute for the La³⁺ ones in two types of sites. The first-principle calculations for undoped NLSO reveal an indirect bandgap of 5.06 eV. The photoluminescence properties were investigated in detail through the measurements of the emission spectra and luminescence decay curves. The NLSO:0.2Dy phosphor exhibited the typical Dy³⁺ emission corresponding to $^4F_{9/2} \rightarrow ^6H_J$ transitions, among which the hypersensitive electric-dipole transition $^4F_{9/2} \rightarrow ^6H_{13/2}$ (571 nm) dominates in the spectrum leading to yellow emission color with CIE chromaticity coordinates of (0.469, 0.495) and a correlated color temperature of 3150 K. The concentration quenching mechanism for Dy³⁺ ions was investigated. Excellent thermal stability was found for this new apatite phosphor. The obtained results indicated that NLSO:xDy apatites are promising as potential yellow emitting phosphors for applications in w-LEDs.

Keywords: orthosilicate oxyapatite; crystal structure; dysprosium ions; yellow phosphor; luminescence.

1. Introduction

Compounds belonging to the structural family of apatite are well known for applications exploiting their luminescent properties [1–4]. They have a general chemical formula $A_{10}(\text{MO}_4)_6\text{X}_2$, where A is a metal cation that can be monovalent (Na^+ , Li^+), divalent (Ca^{2+} , Sr^{2+} , Mg^{2+}) or trivalent (e.g., a rare-earth ion, RE^{3+}); X represents anions (F^- , Cl^- , Br^- , O^{2-} , etc.) and MO_4 is an anionic group (PO_4 , SiO_4 , GeO_4 , etc.). Apatites crystallize in the hexagonal class with space group $P6_3/m$ [5]. Among them, rare-earth orthosilicate oxyapatites with general formula $\text{ARE}_9(\text{SiO}_4)_6\text{O}_2$ appear particularly attractive as luminescent host matrices due to their rigid crystalline structure and excellent thermal and chemical stability [6]. For these $\text{ARE}_9(\text{SiO}_4)_6\text{O}_2$ compounds, two cationic sites exist: one with C_3 point symmetry, partially occupied by RE^{3+} ions (site occupancy is 3/4) and univalent A^+ cations (site occupancy is 1/4) and it is IX-fold coordinated resulting in a distorted 3-fold capped trigonal prism geometry, while the second cationic site has C_s symmetry and is populated only by RE^{3+} ions being VII-fold coordinated resulting in a distorted pentagonal bipyramid geometry.

White light-emitting diodes (w-LEDs) play an important role in the field of luminescence and lighting technology. They are replacing the old incandescent and fluorescent lamps owing to their high efficiency and long lifecycle. The approach of combining yellow phosphors and blue InGaN diodes is widely used to achieve white light: blue light is partially absorbed by the phosphor emitting yellow luminescence, and the complementary blue and yellow emissions are mixed in appropriate proportions to generate white light in a compact w-LED [7]. It is thus relevant to search for novel efficient yellow-emitting luminescent materials.

Recently, multiple studies were dedicated to luminescent properties of RE^{3+} -doped orthosilicate oxyapatite compounds [8–11]. Among the activator RE^{3+} ions, dysprosium ions (Dy^{3+}) are attractive for achieving yellow emission. The $^4\text{F}_{9/2} \rightarrow ^6\text{H}_{13/2}$ and $^4\text{F}_{9/2} \rightarrow ^6\text{H}_{15/2}$ transitions of Dy^{3+} fall in the yellow and blue spectral ranges, of which the $^4\text{F}_{9/2} \rightarrow ^6\text{H}_{13/2}$ one is known to be hypersensitive to the crystal field (as $\Delta L = 2$, $\Delta J = 2$) [12–14]. Hence, the yellow / blue (Y/B) emission ratio may be varied via alteration of the structure of the host matrix and the doping level. For example, if Dy^{3+} locates at a low symmetry site, the emission intensity of the $^4\text{F}_{9/2} \rightarrow ^6\text{H}_{13/2}$ transition is stronger than that of the $^4\text{F}_{9/2} \rightarrow ^6\text{H}_{15/2}$ one (leading to yellow luminescence), and vice-versa. Theoretically, the emission color of Dy^{3+} in an appropriate host can be tuned from blue to yellow depending on the chemical environment that surrounds Dy^{3+} . In earlier investigations, the pumping sources of Dy^{3+} -activated materials were all ultraviolet ones (e.g., 254, 349, 359 nm), while blue light is only popular in recent years.

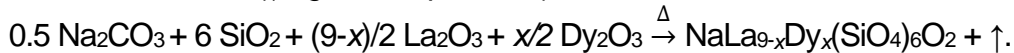
Based on these considerations, Dy^{3+} -doped phosphors have potential application in the field of w-LEDs. So far, most of the reports have focused on the ability of Dy^{3+} -activated materials, such as $\text{Ca}_{2.85}\text{Li}_{0.15}(\text{PO}_4)_{1.85}(\text{SO}_4)_{0.15}$ [15], $\text{Ca}_{0.7}\text{Y}_{0.3}\text{Ti}_{0.7}\text{Al}_{0.3}\text{O}_3$ [16], $\text{NaBi}(\text{MoO}_4)_2$ [17] or $\text{Ca}_2\text{Y}_8(\text{SiO}_4)_6\text{O}_2$ [18], to emit white light. However, there are rare studies on Dy^{3+} -doped phosphors for yellow light applications.

The present work puts emphasis on the apatite family. We have chosen $\text{NaLa}_9(\text{SiO}_4)_6\text{O}_2$ (abbreviated as NLSO) as a host material. Several similar orthosilicate oxyapatites doped with rare-earth ions $\text{ARE}_9(\text{SiO}_4)_6\text{O}_2$ (where A = Li or Na; RE = Y, La or Gd) have been studied previously. Chuai *et al.* investigated the luminescent properties of $\text{NaY}_9(\text{SiO}_4)_6\text{O}_2$ oxyapatite codoped with Eu^{3+} , Tb^{3+} , Dy^{3+} and Pb^{2+} [19]. Lv *et al.* synthesized a series of singly-doped (Ce^{3+} , Tb^{3+} or Eu^{3+}) and codoped (Ce^{3+} , Tb^{3+} and Ce^{3+} , Mn^{2+}) $\text{NaY}_9(\text{SiO}_4)_6\text{O}_2$ phosphors by high-temperature solid-state reaction and studied their structure and luminescent properties [20]. There are no reports on photoluminescent properties of Dy^{3+} -activated NLSO phosphors, to the best of our knowledge. In the present work, such materials were elaborated for the first time.

2. Experimental

2.1. Synthesis of the phosphors

The $\text{NaLa}_{9-x}\text{Dy}_x(\text{SiO}_4)_6\text{O}_2$ (abbreviated: NLSO: $x\text{Dy}$), where $x = 0, 0.01, 0.05, 0.075, 0.1, 0.15, 0.2, 0.25$ and 0.3) phosphors were synthesized by conventional high temperature solid-state reaction. High-purity powders of Na_2CO_3 (A.R. 99.5%), SiO_2 (A.R. 99.9%), La_2O_3 (A.R. 99.9%) and Dy_2O_3 (A.R. 99.5%) were used as starting materials without further purification. According to the stoichiometric ratio, the corresponding powders were weighed and thoroughly ground for about 60 minutes in an agate mortar with presence of small quantity of ethanol to achieve uniformity. Afterwards, these mixtures were sintered at $1100\text{ }^\circ\text{C}$ for 8 h with a heating ratio of $5\text{ }^\circ\text{C}/\text{min}$ to obtain the NLSO: $x\text{Dy}$ phase. The equivalent chemical reaction is shown below (\uparrow - gaseous products):



2.2. Characterization methods

The X-ray powder diffraction (XRD) patterns for the entire NLSO: $x\text{Dy}$ ($x = 0 - 0.3$) series were collected at room-temperature (RT) using a Shimadzu XRD-6000 diffractometer in the Bragg-Brentano geometry. This instrument was equipped with a Cu X-ray source, a scintillation counter as a detector, and a Ni filter to eliminate the K_β radiation. The instrument was operated at a tube voltage of 40 kV and a tube current of 40 mA. The diffraction data for all the samples were registered in the 2θ angular range of $10 - 70^\circ$ at a scan speed of $2^\circ/\text{min}$ and a scan step spacing of 0.02° .

The morphology and size of the particles were studied by transmission electron microscopy (TEM) using a JEOL 1011 microscope. The composition of the samples was determined by electron dispersive X-ray spectroscopy (EDX) using a field emission scanning electron microscope, FE-SEM (Thermo scientific, model scios2) combined with a Thermo Scientific micro-analyzer with Pathfinder software.

The Raman spectra were measured using a Renishaw InVia confocal Raman microscope equipped with an edge filter, a $50\times$ objective (Leica), and an Ar^+ ion laser as excitation source ($\lambda_{\text{exc}} = 514\text{ nm}$). Fourier transform infrared spectroscopy (FTIR) analysis of the samples was performed using a Nicolet 380 FTIR spectrophotometer.

The RT reflectance spectra in the $200\text{-}600\text{ nm}$ range were measured using a CARY 5000 (Varian) spectrophotometer. The RT excitation spectra were measured using a Horiba Spectrofluorimeter (QuantaMaster series) with a spectral resolution of 0.4 nm . The RT luminescence spectra were measured using the same confocal Raman microscope using another line of the Ar^+ ion laser ($\lambda_{\text{exc}} = 457\text{ nm}$). For temperature-dependent measurements in the $25 - 400\text{ }^\circ\text{C}$ range, we used a Linkam TMS94 temperature controller. The RT luminescence decay curves were measured using a Cary Eclipse fluorescence spectrometer.

2.3. DFT calculations

The electronic structure was established by the density-functional theory (DFT) method using the Cambridge Serial Total Energy Package (CASTEP) code [21]. The generalized gradient approximation (GGA) [22], under the Perdew-Burke-Ernzerhof (PBE) formulation [23], was chosen as a theoretical basis of the density function. A norm-conserving pseudopotential (NCP) [24] was used to simulate orbital electrons. The cutoff energy of plane-wave basis was 789.10 eV . The k-point sampling scheme of the $3\times 3\times 3$ Monkhorst-Pack grid was used. The other calculation parameters and convergent criteria were the default values in CASTEP.

3. Results and discussion

3.1. Structure analysis

The XRD patterns of NLSO:*x*Dy phosphors (for *x* in the range of 0 – 0.3) are shown in Fig. 1(a). All the observed diffraction peaks matched well with the standard powder diffraction file (PDF) card JCPDS #96-400-1780 corresponding to lanthanum silicate oxyapatite, $\text{La}_{9.50}\text{Si}_{5.87}\text{O}_{26}$, Fig. 1(b). No other diffraction peaks of any impurity phases were observed, stating that all the samples are of single-phase nature. The NLSO:*x*Dy phosphors crystallize in the hexagonal class with space group $P6_3/m - C_{2h}^{26}$, No. 176 and point group $6/m$. The doping levels studied with Dy^{3+} does not alter the structure of the material.

To better understand the structure of NLSO:*x*Dy and the incorporation behavior of Dy^{3+} ions in the NLSO host matrix, the Rietveld refinement of undoped and Dy^{3+} -doped samples (NLSO:0.1Dy) was carried out using match3! software, Fig. 2. The refinement parameters are listed in Table 1. The crystal structure of $\text{LiY}_{9-x}\text{Ce}_x(\text{SiO}_4)_6\text{O}_2$ [25] was taken as a starting model for the refinement. The calculated patterns agree well with the experimental profiles. For undoped NLSO, the determined lattice parameters are $a = b = 9.6917(3) \text{ \AA}$ and $c = 7.1836(4) \text{ \AA}$, $\gamma = 120^\circ$ (the number of the units formula $Z = 1$), the volume of the unit-cell $V = 584.357 \text{ \AA}^3$ and the calculated density $\rho_{\text{calc}} = 5.279 \text{ g/cm}^3$. The reliability factors of the refinement are $R_{\text{wp}} = 13.8\%$, $R_{\text{exp}} = 9.43\%$ and the chi-squared $\chi^2 = (R_{\text{wp}}/R_{\text{exp}})^2$ is 2.14 indicating good convergence of the fit. The obtained fractional atomic coordinates, site occupancy factors and isotropic thermal factors for both undoped and Dy^{3+} -doped samples are summarized in Table 2.

Based on the results of the Rietveld refinement, a projection of the crystal structure was drawn, as shown in Fig. 3. For undoped NLSO, the cations (La^{3+} , Na^+ , Si^{4+}) occupy Wyckoff positions $4f$ and $6h$. The $4f$ site with C_3 point symmetry is occupied by La^{3+} and Na^+ cations coordinated by nine oxygen atoms, while the $6h$ site with C_s point symmetry is mainly occupied by only La^{3+} ions coordinated by seven oxygen atoms. The isolated $[\text{SiO}_4]^{4-}$ tetrahedra are linked by cation polyhedra $[\text{Na}|\text{LaO}_9]$ and $[\text{LaO}_6]$. A particular structural feature of oxyapatites containing rare-earths ions is the presence of the so-called free oxygen (O_4), which does not link to any silicon tetrahedron and is very close to the $6h$ sites. Its charge is strongly undercompensated by the neighboring cations. This leads to the following principle of site occupancy in silicate apatites formulated by Blasse *et al.* [26]: it is very unfavorable to have cations of large radius and small charge (e.g., Na^+) in the $6h$ sites.

As evidenced by the XRD studies, the Dy^{3+} ions successfully incorporate into the NLSO host lattice. They are expected to replace the host-forming trivalent cations, La^{3+} , in two types of sites with point symmetries C_3 (C.N. = IX) and C_s (C.N. = VII), where C.N. is the coordination number by oxygen. The ionic radii of Dy^{3+} dopant ions are $R_{\text{Dy(IX)}} = 1.083 \text{ \AA}$ and $R_{\text{Dy(VII)}} = 0.97 \text{ \AA}$ being smaller than those for the host-forming La^{3+} cations, $R_{\text{La(IX)}} = 1.216 \text{ \AA}$ and $R_{\text{La(VII)}} = 1.1 \text{ \AA}$ [27]. Thus, it is expected that the Dy^{3+} doping will lead to the shrinkage of the unit-cell volume. This is well evidenced by focusing on the $(hkl) = (002)$ diffraction peak in the measured XRD patterns of the NLSO:*x*Dy phosphors, cf. Fig. 1(c), whose position is gradually shifted to larger diffraction angles 2θ as the concentration of Dy^{3+} ions increases. Indeed, the lattice parameters for the sample NLSO:0.3Dy are $a = b = 9.6651(1) \text{ \AA}$ and $c = 7.1756(4) \text{ \AA}$, $\gamma = 120^\circ$ which are smaller than those for undoped NLSO.

The mean size of the crystallites D_{hkl} can be estimated using the Debye-Scherrer formula [28]:

$$D_{hkl} = \frac{0.9\lambda}{\beta \cos(\theta)}, \quad (1)$$

where, λ is the wavelength of X-rays (1.54056 \AA), β is the full width at half maximum (FWHM) of the diffraction peak and θ is the peak diffraction angle. The most intense reflections (211) were considered for this calculation, Table 3. As the Dy^{3+} doping concentration increases, D_{hkl} decreases slightly from 132 nm (for undoped NLSO) to 113 nm (for NLSO:0.3Dy).

3.2. IR and Raman spectroscopy

IR and Raman spectra of NLSO:*x*Dy (*x* = 0, 0.1, 0.2 and 0.3) oxyapatites are shown in Fig. 4. For the IR spectra recorded in the 400-1200 cm⁻¹ range, Fig. 4(a), the typical bands of the SiO₄ groups are revealed at 958-975 cm⁻¹ and assigned to antisymmetric stretching modes (ν_{as}), those at 862-908 cm⁻¹ - to symmetric stretching mode (ν_s), the band around 539 cm⁻¹ is referred to antisymmetric bending modes (δ_{as}), and those at 454-487 cm⁻¹ - to symmetric bending modes (δ_s) of the SiO₄ tetrahedra [29,30]. The identification of these spectral components indicates the existence of orthosilicate groups. The observed large bandwidths, especially for the ν_s mode, are ascribed to distortion of isolated SiO₄ groups from the ideal T_d symmetry [31]. The intense band at 656 cm⁻¹ is attributed to antisymmetric and symmetric stretching vibrations of the Si–O–Si bands.

The bands observed in the Raman spectra, Fig. 4(b), recorded in the range of 70-1200 cm⁻¹, have been assigned to modes of silicate groups in the apatite structure [32,33]. The Raman spectra contained bands grouped in two distinct regions. In the high-frequency range, the intense band at 850 cm⁻¹ is ascribed to the symmetric stretching mode ν_s of SiO₄ tetrahedra and the weak bands at 930-945 cm⁻¹ - to the corresponding asymmetric stretching mode ν_{as} . At intermediate frequencies above 325 cm⁻¹, the band at 388 cm⁻¹ is assigned to the symmetric bending mode δ_s and those at 521-565 cm⁻¹ - to the asymmetric bending mode δ_{as} of the SiO₄ groups. The bands at smaller frequencies are due to external modes [34]. For the sample with *x* = 0.3, we have observed a slight broadening and red shifting of the stretching bands due to the cation disordering and distortion of the SiO₄ tetrahedra.

3.3. Morphology and composition

The morphology and microstructure of NLSO:*x*Dy (*x* = 0 and 0.3) phosphors were investigated by TEM and FESEM. TEM displays spherical nanoparticles, Fig. 5(a,b), with a relatively broad size distribution as shown in Fig. 5(c,d). Small particles are agglomerated forming bigger crystallites. The mean size of the nanoparticles determined by the linear intersect method decreases from 175 nm for undoped NLSO to 115 nm for NSLO:0.1Dy which is in good agreement with the XRD findings.

Figure 6(a,b) presents the EDX spectra of undoped NLSO and NLSO:0.1Dy phosphors verifying the presence of Na, La, Si, O (in both samples) and Dy (in doped sample) elements. The EDX element mapping for the NLSO:0.3Dy phosphor is shown in Fig. 6(c). This analysis confirms a uniform distribution of Dy³⁺ ions over La³⁺ sites in the host lattice.

3.4. Bandgap and electronic structure

The DFT method was used to calculate the energy band structure and the density of states (DOS) of the phosphor host, Fig. 8. The top of the valence band (VB) is located at the high symmetry point G of the Brillouin zone, while the bottom of the conduction band (CB) is located at another point M, indicating that NLSO is an indirect bandgap material. The calculated bandgap E_g is 5.06 eV. The wide bandgap nature of NLSO is attractive for its applications as a matrix for doping with luminescent centers and for improving the thermal stability of the material.

Figure 10 shows the partial densities of states (PDOS) for O, La, Si and Na. The band located at -17.3 eV is attributed to the state O_2s. Near the Fermi level (energy equal to zero), in the VB, the main peak localized at -2.5 eV is mostly contributed by the O_2p state. The bottom of the CB located at around 4.95 eV mainly originates from the La_5d state. Thus, the bandgap of NLSO is attributed to the charge transfer from the O_2p to the La_5d state.

The diffuse reflectance spectra of undoped NLSO and NLSO:0.1Dy samples, Fig. 9(a), exhibit a strong rise of absorption in the UV, around 220 nm, corresponding to the band edge

absorption of the NLSO host. The Dy-O-P charge transfer band (CTB) band for NLSO:0.1Dy is detected at 209 nm.

The experimental bandgap energy E_g can be derived using the so-called Tauc plot [35]:

$$(\alpha_{\text{abs}} \cdot h\nu_{\text{ph}})^n = A \cdot (h\nu_{\text{ph}} - E_g), \quad (2)$$

where $h\nu_{\text{ph}}$ is the photon energy, α_{abs} is the absorption coefficient, n is the parameter depending on the transition type ($n = 1/2, 2, 3/2$ or 3 for allowed direct, allowed indirect, forbidden direct and forbidden indirect electronic transitions, respectively). According to the DFT analysis, NLSO is an indirect band gap material ($n = 2$). From the corresponding Tauc plot of the NLSO sample shown in Fig. 9(b), we achieve $E_g = 5.84$ eV, which is slightly higher than the calculated value. The reason behind this underestimation is the discontinuity of the exchange correlation energy function [36]. The measured optical bandgap for the Dy-doped sample NLSO:0.1Dy (5.35 eV) is slightly smaller than that for the host material.

3.5. Photoluminescence

Figure 11(a) shows the measured RT excitation spectra of the NLSO:0.2Dy phosphor. The emission at two wavelengths was monitored: 571 nm and 478 nm. The corresponding excitation spectra are very similar. They exhibit several bands peaking at ~323, 348, 363/366, 386, 425 and 452 nm corresponding to transitions from the ground-state ${}^6\text{H}_{15/2}$ to the higher-lying excited-states ${}^6\text{P}_{3/2}$, ${}^6\text{P}_{7/2}$, ${}^6\text{P}_{5/2}$, ${}^4\text{I}_{13/2}$, ${}^4\text{G}_{11/2}$ and ${}^4\text{I}_{15/2}$, respectively. In particular, the broad band peaking at ~452 nm (the ${}^6\text{H}_{15/2} \rightarrow {}^4\text{I}_{15/2}$ transition in absorption) is suitable for using commercial blue diode lasers as excitation sources of NLSO:xDy phosphors.

The RT photoluminescence (PL) spectra of NLSO:xDy phosphors as a function of Dy^{3+} doping level are shown in Fig. 12(a) (measured for $\lambda_{\text{exc}} = 457$ nm). The spectra contain three intense bands at ~478, 571 and 662 nm originating from the ${}^4\text{F}_{9/2} \rightarrow {}^6\text{H}_{15/2}$, ${}^4\text{F}_{9/2} \rightarrow {}^6\text{H}_{13/2}$ and ${}^4\text{F}_{9/2} \rightarrow {}^6\text{H}_{11/2}$ electronic transitions of Dy^{3+} ions, respectively. It is known that the ${}^4\text{F}_{9/2} \rightarrow {}^6\text{H}_{13/2}$ Dy^{3+} transition is a hypersensitive one. When Dy^{3+} ions are located in low-symmetry sites, the yellow emission dominates in the PL spectrum, otherwise the blue emission (${}^4\text{F}_{9/2} \rightarrow {}^6\text{H}_{15/2}$) is dominant [37,38]. For the studied material, the intensity of the yellow emission is stronger than that of the blue emission, indicating that Dy^{3+} ions are located at low symmetry sites in agreement with the XRD findings (namely, the C_3 and C_s symmetry sites).

As for the concentration dependence of the PL intensity, it first increases and reaches a maximum at $x = 0.2$ and then drops owing to the concentration quenching, see Fig. 12(b). The concentration quenching is driven by the process of non-radiative energy transfer between neighboring Dy^{3+} ions when the doping concentration attains a critical value [39,40]. To characterize the concentration quenching of the NLSO:xDy phosphor, the critical distance of the energy transfer R_c was estimated using the equation proposed by Blasse [41,42]:

$$R_c \approx 2 \left[\frac{3V}{4\pi x_c N} \right]^{1/3}, \quad (3)$$

where V is the volume of the unit-cell, N is the number of host cations in the unit-cell, x_c is the atom fraction of activator at which the quenching occurs. For the NLSO:0.2Dy sample, $N = 1$, $V = 582.589 \text{ \AA}^3$ (from XRD data) and $x_c = 0.2$. According to Eq. (3), R_c amounts to 17.7 \AA , which is in agreement with the previously reported values for Dy^{3+} -activated apatite phosphors, such as $\text{Ca}_9\text{La}(\text{PO}_4)_5(\text{GeO}_4)\text{F}_2$ ($R_c = 17.23 \text{ \AA}$) [43] and $\text{Ca}_5\text{Y}_3\text{Na}_2(\text{PO}_4)_5(\text{SiO}_4)\text{F}_2$ ($R_c = 17.05 \text{ \AA}$) [44]. Exchange and multipolar interactions are the two main effects responsible for the resonant energy transfer. The probability of energy transfer via the exchange interaction mechanism for distances exceeding 5 \AA is very low [45]. As for the multipolar interactions, their type can be determined from the following equation [46]:

$$\log\left(\frac{I}{x}\right) = K - \frac{\theta}{3} \log(x), \quad (4)$$

where I is the PL intensity, x is the concentration of the activator which is greater than the critical concentration, K is a constant specific for the host material and θ is a multipole character function: $\theta = 6, 8$ or 10 for dipole-dipole (d-d), dipole-quadrupole (d-q) or quadrupole-quadrupole (q-q) interactions, respectively.

The inset in Fig. 12(b) shows the application of Eq. (4) to the studied material (for $x > 0.2$). The ${}^4F_{9/2} \rightarrow {}^6H_{13/2}$ transition of Dy^{3+} ions was analyzed. The slope of the dependence of $\log(I/x)$ on $\log(x)$ is -1.22 ± 0.05 , equivalent to $\theta = 3.63$ suggesting mainly d-d interactions.

The scheme of energy-levels of Dy^{3+} ions is shown in Fig. 11(b). The excitation of Dy^{3+} ions at 457 nm populates the short-living ${}^4I_{15/2}$ excited-state. The excited ions experience an efficient multi-phonon non-radiative (NR) relaxation to the lower-lying metastable ${}^4F_{9/2}$ state. The visible emissions of Dy^{3+} ions originate from transitions from this state terminating at the ground-state (${}^6H_{15/2}$, in the blue), ${}^6H_{13/2}$ (in the yellow) and ${}^6H_{11/2}$ (in the red).

3.6. Luminescence decay

Figure 13(a) shows the luminescence decay curves for NLSO: x Dy samples plotted in a semi-log scale. The emission was monitored at 571 nm (decay from the metastable ${}^4F_{9/2}$ excited state). The decay curves are clearly not single exponential for all the studied samples. This agrees with the accommodation of Dy^{3+} ions in two different crystallographic sites with different symmetry and coordination. The application of the bi-exponential fit to the decay curve measured for the sample with the lowest studied Dy^{3+} doping level ($x = 0.01$, corresponding to weak concentration quenching and weak ion interactions) yields the lifetimes $\tau_1 = 0.27 \pm 0.03$ ms and $\tau_2 = 0.8 \pm 0.02$ ms.

For all the decay curves, we have also calculated the mean decay time $\langle \tau_{lum} \rangle$, as shown in Fig. 13(b). With increasing the Dy^{3+} doping level x from 0.01 to 0.3, $\langle \tau_{lum} \rangle$ tends to decrease from 0.758 ms to 0.523 ms. A similar behavior was observed in [45] for another Dy^{3+} activated apatite phosphor, $Ba_2Y_{3-3x}Dy_{3x}(SiO_4)_3F$, for which $\langle \tau_{lum} \rangle$ decreased from 1.096 ms to 0.785 ms for x from 0.005 to 0.08. The dependence in Fig. 13(c) is not completely monotonous as certain redistribution of Dy^{3+} ions over the lattice sites is expected with increasing the Dy^{3+} doping level, as evidenced by slight changes in the PL spectra.

The decrease of the ${}^4F_{9/2}$ Dy^{3+} lifetime with the doping level is well known and is related to cross-relaxation (CR) among adjacent ions at increasing doping levels. The CR processes are shown in Fig. 11(b). The main CR channels are (i) ${}^4F_{9/2} + {}^6H_{15/2} \rightarrow {}^4F_{1/2} + {}^6H_{9/2}$, ${}^4F_{9/2} + {}^6H_{15/2} \rightarrow {}^6F_{5/2} + {}^6H_{7/2}$ and ${}^4F_{9/2} + {}^6H_{15/2} \rightarrow {}^6F_{5/2} + {}^6H_{5/2}$ [47]. All these processes are phonon-assisted. With increasing the Dy^{3+} doping level in NLSO, the distances between the activator ions decrease leading to increasing CR probability, which shortens the lifetime.

3.7. Temperature-dependent luminescent properties

Thermal stability is an important factor for practical applications of phosphors. During continuous excitation, the temperature of the luminophore rises due to the heat release related to NR transitions of the activator ions, energy transfer to defects and impurities, as well as host absorption, which deteriorates the PL efficiency. A thermal stability test was carried out for the NLSO:0.2Dy sample in the temperature range of RT - 400 °C, as shown in Fig. 14. The PL intensity decreases with temperature. It is reduced to ~65% at 200 °C and to ~17% at 400 °C with respect to the initial intensity at RT. A schematic diagram explaining the reduction in the PL intensity is shown in Fig. 15(a), showing how Dy^{3+} ground electrons excited by blue light can return to the ground state via radiative transitions in the blue, yellow and red spectral ranges. With the temperature rise, the interaction of activator ions with thermally active phonons of the host matrix promotes the electrons to overcome the activation energy E_a and reach the intersection of the ground- and excited states, called the P-point.

The electrons then return to the ground state non-radiatively (via g). The activation energy, E_a , was derived using the Arrhenius-type activation model [48,49]:

$$I(T) = I_0 \left(1 + c \exp\left(-\frac{E_a}{kT}\right) \right)^{-1}, \quad (5)$$

where I is the PL intensity at a given temperature T , I_0 is its value at RT, c is a constant, k is the Boltzmann constant and E_a is the activation energy. Figure 15(b) shows the plot of $\ln((I/I_0) - 1)$ versus $1/(kT)$ for the NLSO:0.2Dy sample. The linear fit of the experimental points yields an activation energy $E_a = 0.23 \pm 0.015$ eV. Consequently, the studied phosphor possesses good thermal stability, which provides an excellent possibility for applications in w-LEDs.

3.8. Chromaticity coordinates and CCT

Figure 16 shows the CIE (*Commission Internationale de l'Eclairage*) 1931 color space together with the color coordinates (x , y) of luminescence of the NLSO: x Dy phosphors. The (x , y) coordinates were calculated from the PL spectra and their values are listed in Table 4. For the sample with highest emission intensity ($x = 0.2$), the chromaticity coordinates are (0.469, 0.495) corresponding to a dominant wavelength λ_d of 570 nm falling in the yellow range with a color purity p of 98%. With increasing the Dy³⁺ doping level, there is a tendency for shifting the (x , y) coordinates towards orange emission and increasing the color purity.

The correlated color temperature (CCT) was calculated using the McCamy's empirical formula [50]:

$$\text{CCT} = -437n^3 + 3601n^2 - 6861n + 5514.31 \text{ (K)}, \quad (6)$$

where $n = (x - x_e)/(y - y_e)$ and $x_e = 0.332$, $y_e = 0.186$ are the coordinates of the epicenter of convergence. The resulting values of CCT are listed in Table 4. For the sample with $x = 0.2$, CCT amounts to 3150 K.

Table 5 presents a comparison of the emission properties of several Dy³⁺ activated apatite phosphors studied so far. Note that the color of emission changes from yellow to white, depending on the actual composition of the phosphor host. In our case, the yellow / blue (Y/B) emission ratio is relatively high as compared to other phosphors, which leads to a strong yellow luminescence.

4. Conclusions

In conclusion, by using the traditional solid-state reaction, novel single-phase yellow-emitting NaLa₉(SiO₄)₆O₂: x Dy³⁺ phosphors were synthesized. A systematic study of the crystal structure, morphology, Raman and IR spectra and luminescent properties of the synthesized phosphors was performed. The X-ray diffraction indicated that the as-prepared phosphors crystallize in the hexagonal system with space group $P6_3/m$ and, that the dopant Dy³⁺ ions occupy two non-equivalent crystallographic sites with the symmetries C_s and C_3 . The DFT calculations indicated a wide indirect bandgap of 5.06 eV. The luminescence spectra of the phosphors are dominated by the $^4F_{9/2} \rightarrow ^6H_{13/2}$ band at ~571 nm which determines the yellow emission color. The luminescence decay curves exhibit a double exponential shape confirming the multi-site nature of the material. The mean luminescence lifetime of the $^4F_{9/2}$ Dy³⁺ state is 0.758 ms at low doping level and it shows relatively weak dependence on the Dy³⁺ concentration. The phosphor composition with $x = 0.2$ corresponds to the maximum emission intensity. The critical radius R_c is calculated to be 17.66 Å, indicating that the concentration quenching is probably caused by d-d interactions. The CIE chromaticity coordinates were calculated falling into the yellow color region for all the studied Dy³⁺ doping levels. The corresponding CCT values are in the range 3398 - 3152 K. Finally, temperature-dependent luminescence measurements indicated excellent thermal stability. Combining all the results, we conclude that NLSO:Dy might serve as yellow-emitting phosphors for w-LEDs.

Acknowledgments

This work was supported by Spanish Government, Ministry of Science and Innovation (project No. PID2019-108543RB-I00) and by Generalitat de Catalunya (project No. 2017SGR755). This research article has been possible with the support of the Secretaria d'Universitats i Recerca del Departament d'Empresa i Coneixement de la Generalitat de Catalunya, the European Union (UE) and the European Social Fund (ESF) (2020 FI-B 00522).

References

- [1] Y.I. Jeon, L. Krishna Bharat, J.S. Yu, Synthesis and luminescence properties of $\text{Eu}^{3+}/\text{Dy}^{3+}$ ions co-doped $\text{Ca}_2\text{La}_8(\text{GeO}_4)_6\text{O}_2$ phosphors for white-light applications, *J. Alloys Compd.* 620 (2015) 263–268.
- [2] Q. Wang, Z. Ci, Y. Wang, G. Zhu, Y. Wen, Y. Shi, Crystal structure, photoluminescence properties and energy transfer of Ce^{3+} , Mn^{2+} co-activated $\text{Ca}_8\text{NaGd}(\text{PO}_4)_6\text{F}_2$ phosphor, *Mater. Res. Bull.* 48 (2013) 1065–1070.
- [3] H. Liu, Y. Luo, Z. Mao, L. Liao, Z. Xia, A novel single-composition trichromatic white-emitting $\text{Sr}_{3.5}\text{Y}_{6.5}\text{O}_2(\text{PO}_4)_{1.5}(\text{SiO}_4)_{4.5}:\text{Ce}^{3+}/\text{Tb}^{3+}/\text{Mn}^{2+}$ phosphor: Synthesis, luminescent properties and applications for white LEDs, *J. Mater. Chem. C* 2 (2014) 1619–1627.
- [4] M. Tong, Y. Liang, G. Li, Z. Xia, M. Zhang, F. Yang, Q. Wang, Luminescent properties of single Dy^{3+} ions activated $\text{Ca}_3\text{Gd}_7(\text{PO}_4)(\text{SiO}_4)_5\text{O}_2$ phosphor, *Opt. Mater.* 36 (2014) 1566–1570.
- [5] J. Cheng, J. Zhang, X. Bian, Z. Zhai, J. Shi, Photoluminescence properties, Judd-Ofelt analysis, and optical temperature sensing of Eu^{3+} -doped $\text{Ca}_3\text{La}_7(\text{SiO}_4)_5(\text{PO}_4)\text{O}_2$ luminescent materials, *Spectrochim. Acta A* 230 (2020) 118057.
- [6] S. Wang, Wei-Wang, X. jun Zhou, Y. jie Li, G. chao Hua, Z. xuan Li, D. jian Wang, Z. yong Mao, Z. wei Zhang, Ying-Zhao, Comparative study of the luminescence properties of $\text{Ca}_{2+x}\text{La}_{8-x}(\text{SiO}_4)_{6-x}(\text{PO}_4)_x\text{O}_2:\text{Eu}^{3+}$ ($x = 0, 2$) red phosphors, *J. Lumin.* 221 (2020) 117043.
- [7] W. Li, G. Fang, Y. Wang, Z. You, J. Li, Z. Zhu, C. Tu, Y. Xu, W. Jie, Luminescent properties of Dy^{3+} activated $\text{LaMgAl}_{11}\text{O}_{19}$ yellow emitting phosphors for application in white-LEDs, *Vacuum.* 188 (2021) 110215.
- [8] J. Zhang, Q. Guo, L. Liao, Y. Wang, M. He, H. Ye, L. Mei, H. Liu, T. Zhou, B. Ma, Structure and luminescence properties of $\text{La}_6\text{Ba}_4(\text{SiO}_4)_6\text{F}_2:\text{Dy}^{3+}$ phosphor with apatite structure, *RSC Adv.* 8 (2018) 38883–38890.
- [9] Q. Guo, B. Ma, L. Liao, M.S. Molokeev, L. Mei, H. Liu, Crystal structure and luminescence properties of novel $\text{Sr}_{10-x}(\text{SiO}_4)_3(\text{SO}_4)_3\text{O}:\text{xEu}^{2+}$ phosphor with apatite structure, *Ceram. Int.* 42 (2016) 11687–11691.
- [10] R. El Ouenzerfi, G. Panczer, C. Goutaudier, M.T. Cohen-Adad, G. Boulon, M. Trabelsi-Ayedi, N. Kbir-Arigoib, Relationships between structural and luminescence properties in Eu^{3+} -doped oxyphosphate-silicate apatite $\text{Ca}_{2+x}\text{La}_{8-x}(\text{SiO}_4)_{6-x}(\text{PO}_4)_x\text{O}_2$, *Opt. Mater.* 16 (2001) 301–310.
- [11] H. Liu, L. Liao, Y. Zhang, T. Zhou, Q. Guo, L. Li, L. Mei, Structure refinement and luminescence properties of a novel apatite-type compound $\text{Mn}_2\text{Gd}_8(\text{SiO}_4)_6\text{O}_2$, *Dye. Pigment.* 140 (2017) 87–91.
- [12] H. Chen, P. Loiseau, G. Aka, Optical properties of Dy^{3+} -doped CaYAlO_4 crystal, *J. Lumin.* 199 (2018) 509–515.
- [13] H. Liu, L. Liao, Q. Guo, D. Yang, L. Mei, $\text{Ca}_9\text{La}(\text{PO}_4)_5(\text{SiO}_4)\text{Cl}_2:\text{Dy}^{3+}$: A white-emitting apatite-type phosphor pumped for n-UV w-LEDs, *J. Lumin.* 181 (2017) 407–410.
- [14] R. Mi, J. Chen, Y. Liu, L. Mei, J. Yuan, Y. Xia, Z. Huang, M. Fang, Crystal structure and luminescence property of a novel single-phase white light emission phosphor $\text{KCaBi}(\text{PO}_4)_2:\text{Dy}^{3+}$, *Mater. Res. Bull.* 86 (2017) 146–152.
- [15] M. Yu, X. Xu, W. Zhang, X. Chen, P. Zhang, Y. Huang, The effect of Sm^{3+} co-doping on

- the luminescence properties of $\text{Ca}_{2.85}\text{Li}_{0.15}(\text{PO}_4)_{1.85}(\text{SO}_4)_{0.15}:\text{Dy}^{3+}$ white-emitting phosphors, *J. Alloys Compd.* 817 (2020) 152761.
- [16] W. Zhang, C. Zou, C. Bao, S. Dai, Y. Huang, L. Wu, K. Qiu, Synthesis and luminescence properties of Eu^{3+} codoped $\text{Ca}_{0.7}\text{Y}_{0.3}\text{Ti}_{0.7}\text{Al}_{0.3}\text{O}_3:\text{Dy}^{3+}$ white-emitting phosphor through sol-gel method, *Powder Technol.* 356 (2019) 661–670.
- [17] W. Li, W. Zhang, W. Li, Y. Gan, P. Zhang, Synthesis and luminescence properties of Eu^{3+} co-doped $\text{NaBi}(\text{MoO}_4)_2:\text{Dy}^{3+}$ phosphors for white light-emitting diodes, *J. Mater. Sci. Mater. Electron.* 30 (2019) 658–666.
- [18] M. Yu, J. Lin, Y.H. Zhou, S.B. Wang, H.J. Zhang, Sol-gel deposition and luminescent properties of oxyapatite $\text{Ca}_2(\text{Y,Gd})_8(\text{SiO}_4)_6\text{O}_2$ phosphor films doped with rare earth and lead ions, *J. Mater. Chem.* 12 (2002) 86–91.
- [19] X.H. Chuai, H.J. Zhang, J. Lin, X.H. Chuai, H.J. Zhang, F.S. Li, S.Z. Lu, J. Lin, S.B. Wang, K. Chi-Chou, Synthesis and luminescence properties of oxyapatite $\text{NaY}_9\text{Si}_6\text{O}_{26}$ doped with Eu^{3+} , Tb^{3+} , Dy^{3+} and Pb^{2+} , *J. Alloys Compd.* 334 (2002) 211–218.
- [20] W. Lv, Y. Jia, W. Lü, Q. Zhao, M. Jiao, B. Shao, H. You, Ce^{3+} , Tb^{3+} , Eu^{3+} , Mn^{2+} -doped and codoped $\text{NaY}_9(\text{SiO}_4)_6\text{O}_2$ phosphors: Luminescence, energy transfer, tunable color properties, *ECS J. Solid State Sci. Technol.* 3 (2014) R9–R13.
- [21] A. Faucher, V. V. Tersikh, R.E. Wasylishen, Feasibility of arsenic and antimony NMR spectroscopy in solids: An investigation of some group 15 compounds, *Solid State Nucl. Magn. Reson.* 61–62 (2014) 54–61.
- [22] M. Zhou, X. Jiang, C. Li, Z. Lin, J. Yao, Y. Wu, The double molybdate $\text{Rb}_2\text{Ba}(\text{MoO}_4)_2$: Synthesis, crystal structure, optical, thermal, vibrational properties, and electronic structure, *Zeitschrift Fur Anorg. Und Allg. Chemie.* 641 (2015) 2321–2325.
- [23] J. Sun, H. Wang, Y. Zhang, Y. Zheng, Z. Xu, R. Liu, Structure and luminescent properties of electrodeposited Eu^{3+} -doped CaF_2 thin films, *Thin Solid Films* 562 (2014) 478–484.
- [24] A.M. Rappe, K.M. Rabe, E. Kaxiras, J.D. Joannopoulos, Optimized pseudopotentials, *Phys. Rev. B.* 41 (1990) 1227–1230.
- [25] W. Zhou, F. Pan, L. Zhou, D. Hou, Y. Huang, Y. Tao, H. Liang, Site Occupancies, Luminescence, and Thermometric Properties of $\text{LiY}_9(\text{SiO}_4)_6\text{O}_2:\text{Ce}^{3+}$ Phosphors, *Inorg. Chem.* 55 (2016) 10415–10424.
- [26] G. Blasse, Influence of local charge compensation on site occupation and luminescence of apatites, *J. Solid State Chem.* 14 (1975) 181–184.
- [27] R.D. Shannon, Revised effective ionic radii and systematic studies of interatomic distances in halides and chalcogenides, *Acta Crystallogr. Sect. A.* 32 (1976) 751–767.
- [28] G. Seeta Rama Raju, H.C. Jung, J.Y. Park, B.K. Moon, R. Balakrishnaiah, J.H. Jeong, J.H. Kim, The influence of sintering temperature on the photoluminescence properties of oxyapatite $\text{Eu}^{3+}:\text{Ca}_2\text{Gd}_8\text{Si}_6\text{O}_{26}$ nanophosphors, *Sensors Actuators, B Chem.* 146 (2010) 395–402.
- [29] K. Boughzala, E. Ben Salem, A. Ben Chrifa, E. Gaudin, K. Bouzouita, Synthesis and characterization of strontium-lanthanum apatites, *Mater. Res. Bull.* 42 (2007) 1221–1229.
- [30] N. Lakshminarasimhan, U. V. Varadaraju, Synthesis and Eu^{3+} luminescence in new oxysilicates, $\text{Ala}_3\text{Bi}(\text{SiO}_4)_3\text{O}$ and $\text{Ala}_2\text{Bi}_2(\text{SiO}_4)_3\text{O}$ [A = Ca, Sr and Ba] with apatite-related structure, *J. Solid State Chem.* 178 (2005) 3284–3292.
- [31] M. Abbassi, R. Ternane, I. Sobrados, A. Madani, M. Trabelsi-Ayadi, J. Sanz, Ionic conductivity of apatite-type solid electrolyte ceramics $\text{Ca}_{2-x}\text{Ba}_x\text{La}_4\text{Bi}_4(\text{SiO}_4)_6\text{O}_2$ ($0 \leq x \leq 2$), *Ceram. Int.* 39 (2013) 9215–9221.
- [32] L. Zhang, H.Q. He, H. Wu, C.Z. Li, S.P. Jiang, Synthesis and characterization of doped $\text{La}_9\text{ASi}_6\text{O}_{26.5}$ (A = Ca, Sr, Ba) oxyapatite electrolyte by a water-based gel-casting route, *Int. J. Hydrogen Energy.* 36 (2011) 6862–6874.
- [33] R. El Ouenzerfi, C. Goutaudier, G. Panczer, B. Moine, M.T. Cohen-Adad, M. Trabelsi-Ayadi, N. Kbir-Arighuib, Investigation of the $\text{CaO}-\text{La}_2\text{O}_3-\text{SiO}_2-\text{P}_2\text{O}_5$ quaternary diagram. Synthesis, existence domain, and characterization of apatitic phosphosilicates, *Solid*

- State Ionics 156 (2003) 209–222.
- [34] A. Orera, E. Kendrick, D.C. Apperley, V.M. Orera, P.R. Slater, Effect of oxygen content on the ^{29}Si NMR, Raman spectra and oxide ion conductivity of the apatite series, $\text{La}_{8+x}\text{Sr}_{2-x}(\text{SiO}_4)_6\text{O}_{2+x/2}$, *J. Chem. Soc. Dalt. Trans.* 9226 (2008) 5296–5301.
- [35] M. Jiao, C. Yang, M. Liu, Q. Xu, Y. Yu, H. You, Mo^{6+} substitution induced band structure regulation and efficient near-UV-excited red emission in $\text{NaLaMg}(\text{W},\text{Mo})\text{O}_6:\text{Eu}$ phosphor, *Opt. Mater. Express* 7 (2017) 2660–2671.
- [36] M. Dalal, J. Dalal, S. Chahar, H. Dahiya, S. Devi, P. Dhankhar, S. Kumar, V.B. Taxak, D. Kumar, S.P. Khatkar, A hybrid treatment of $\text{Ba}_2\text{LaV}_3\text{O}_{11}:\text{Eu}^{3+}$ nanophosphor system: First-principal and experimental investigations into electronic, crystal and the optical structure, *J. Alloys Compd.* 805 (2019) 84–96.
- [37] J.B. Gruber, B. Zandi, U. V. Valiev, S.A. Rakhimov, Energy levels of $\text{Dy}^{3+}(4f^9)$ in orthoaluminate crystals, *J. Appl. Phys.* 94 (2003) 1030–1034.
- [38] S.N. Ogugua, H.C. Swart, O.M. Ntwaeaborwa, White light emitting $\text{LaGdSiO}_5:\text{Dy}^{3+}$ nanophosphors for solid state lighting applications, *Physica B: Cond. Matter* 480 (2016) 131–136.
- [39] Z. Ci, R. Guan, L. Jin, L. Han, J. Zhang, J. Ma, Y. Wang, Host-sensitized white light-emitting phosphor $\text{MgY}_4\text{Si}_3\text{O}_{13}:\text{Dy}^{3+}$ with satisfactory thermal properties for UV-LEDs, *CrystEngComm*. 17 (2015) 4982–4986.
- [40] G. Zhu, S. Xin, A novel blue light pumped yellow-emitting phosphor $\text{RbZnPO}_4:\text{Dy}^{3+}$ with satisfactory color tuning and thermal properties for high-power warm white light emitting diodes, *RSC Adv.* 5 (2015) 10679–106799.
- [41] X. Xiong, X. Yuan, Y. Liang, J. Song, Q. Wu, G. Yin, Photoluminescence properties and energy transfer from Ce^{3+} to Tb^{3+} in Zn_2SiO_4 host, *J. Wuhan Univ. Technol. Mater. Sci. Ed.* 30 (2015) 235–240.
- [42] C.H. Huang, T.M. Chen, Novel yellow-emitting $\text{Sr}_8\text{MgLn}(\text{PO}_4)_7:\text{Eu}^{2+}$ ($\text{Ln} = \text{Y}, \text{La}$) phosphors for applications in white LEDs with excellent color rendering index, *Inorg. Chem.* 50 (2011) 5725–5730.
- [43] Y. Zhang, L. Mei, H. Liu, D. Yang, L. Liao, Z. Huang, Dysprosium doped novel apatite-type white-emitting phosphor $\text{Ca}_9\text{La}(\text{PO}_4)_5(\text{GeO}_4)\text{F}_2$ with satisfactory thermal properties for n-UV w-LEDs, *Dye. Pigment.* 139 (2017) 180–186.
- [44] Y. Wang, Y. Shi, Luminescence properties and thermal quenching behavior of Dy^{3+} activated $\text{Ca}_5\text{Y}_3\text{Na}_2(\text{PO}_4)_5(\text{SiO}_4)\text{F}_2$ phosphor, *J. Mater. Sci. Mater. Electron.* 27 (2016) 10970–10974.
- [45] Y.C. Chiu, W.R. Liu, C.K. Chang, C.C. Liao, Y.T. Yeh, S.M. Jang, T.M. Chen, $\text{Ca}_2\text{PO}_4\text{Cl}:\text{Eu}^{2+}$: An intense near-ultraviolet converting blue phosphor for white light-emitting diodes, *J. Mater. Chem.* 20 (2010) 1755–1758.
- [46] C. Shivakumara, R. Saraf, P. Halappa, White luminescence in Dy^{3+} doped BiOCl phosphors and their Judd-Ofelt analysis, *Dye. Pigment.* 126 (2016) 154–164.
- [47] C. Kränkel, D.T. Marzahl, F. Moglia, G. Huber, P.W. Metz, Out of the blue: semiconductor laser pumped visible rare-earth doped lasers, *Laser Photon. Rev.* 10 (2016) 548–568.
- [48] W. Xiao, X. Zhang, Z. Hao, G.H. Pan, Y. Luo, L. Zhang, J. Zhang, Blue-emitting $\text{K}_2\text{Al}_2\text{B}_2\text{O}_7:\text{Eu}^{2+}$ phosphor with high thermal stability and high color purity for near-UV-pumped white light-emitting diodes, *Inorg. Chem.* 54 (2015) 3189–3195.
- [49] S. Xin, G. Zhu, Enhanced luminescence and abnormal thermal quenching behaviour investigation of $\text{BaHfSi}_3\text{O}_9:\text{Eu}^{2+}$ blue phosphor co-doped with $\text{La}^{3+}\text{-Sc}^{3+}$ ion pairs, *RSC Adv.* 6 (2016) 41755–41760.
- [50] C.S. McCamy, Correlated color temperature as an explicit function of chromaticity coordinates, *Color Res. Appl.* 17 (1992) 142–144.
- [51] Y. Wang, Y. Shi, Luminescence properties and thermal quenching behavior of Dy^{3+} activated $\text{Ca}_5\text{Y}_3\text{Na}_2(\text{PO}_4)_5(\text{SiO}_4)\text{F}_2$ phosphor, *J. Mater. Sci. Mater. Electron.* 27 (2016)

- 10970–10974.
- [52] H. Liu, L. Liao, Q. Guo, D. Yang, L. Mei, $\text{Ca}_9\text{La}(\text{PO}_4)_5(\text{SiO}_4)\text{Cl}_2:\text{Dy}^{3+}$: A white-emitting apatite-type phosphor pumped for n-UV w-LEDs, *J. Lumin.* 181 (2017) 407–410.
- [53] B. Deng, J. Chen, H. Liu, C. song Zhou, Photoluminescence properties of dysprosium doped novel apatite-type $\text{Ba}_2\text{Y}_3(\text{SiO}_4)_3\text{F}$ white-emitting phosphor, *J. Mater. Sci. Mater. Electron.* 30 (2019) 7507–7513.
- [54] J. Zhang, Q. Guo, L. Liao, Y. Wang, M. He, H. Ye, L. Mei, H. Liu, T. Zhou, B. Ma, Structure and luminescence properties of $\text{La}_6\text{Ba}_4(\text{SiO}_4)_6\text{F}_2:\text{Dy}^{3+}$ phosphor with apatite structure, *RSC Adv.* 8 (2018) 38883–38890.
- [55] H. Liu, L. Liao, M.S. Molokeev, Q. Guo, Y. Zhang, L. Mei, A novel single-phase white light emitting phosphor $\text{Ca}_9\text{La}(\text{PO}_4)_5(\text{SiO}_4)\text{F}_2:\text{Dy}^{3+}$: Synthesis, crystal structure and luminescence properties, *RSC Adv.* 6 (2016) 24577–24583.

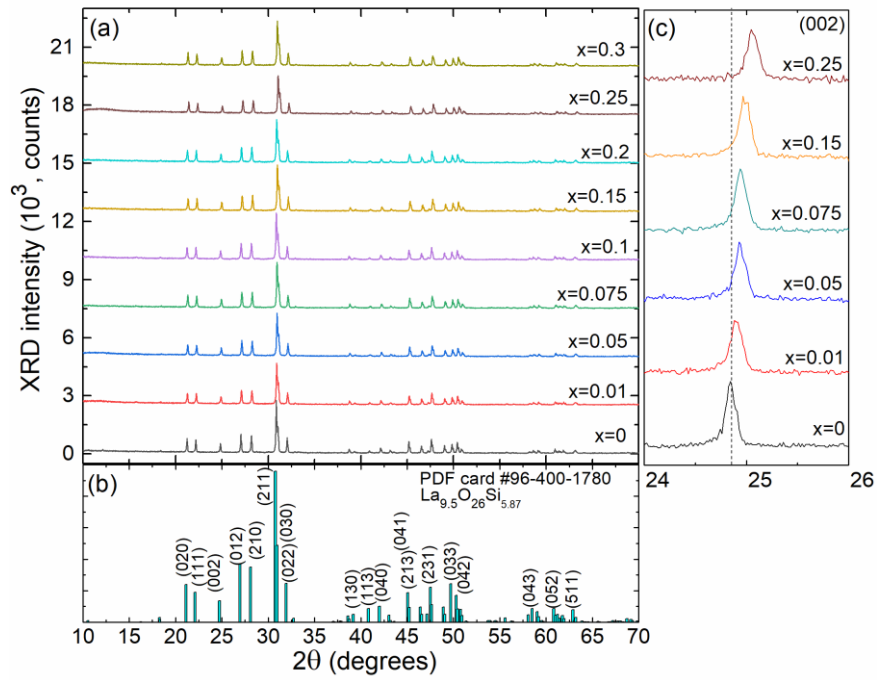


Fig. 1. (a) X-ray diffraction (XRD) patterns of NLSO:*x*Dy (*x* = 0 - 0.3) samples; (b) standard powder diffraction (PDF) card of lanthanum silicate oxyapatite, La_{9.5}O₂₆Si_{5.87}, JCPDS #96-400-1780, *numbers (hkl)* indicate the Miller's indices; (c) Bragg position of the (002) reflection for several doping levels.

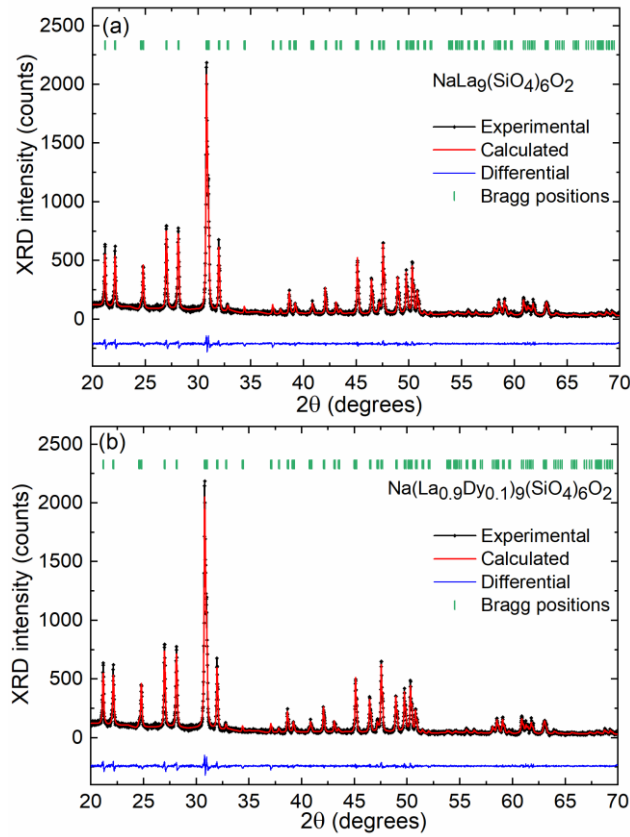


Fig. 2. Rietveld refinement for (a) undoped NLSO and (b) NLSO:0.1Dy samples: experimental (*black*), calculated (*red*) and differential (*green*) patterns, *vertical dashes* – Bragg reflections.

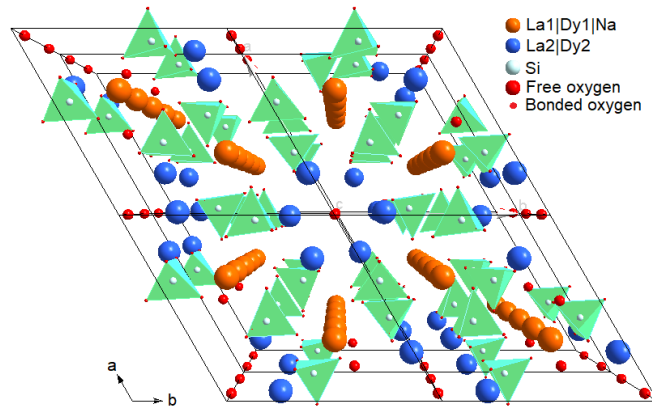


Fig. 3. Projection of the unit cell of the crystal structure of NLSO:*x*Dy on the a-b plane.

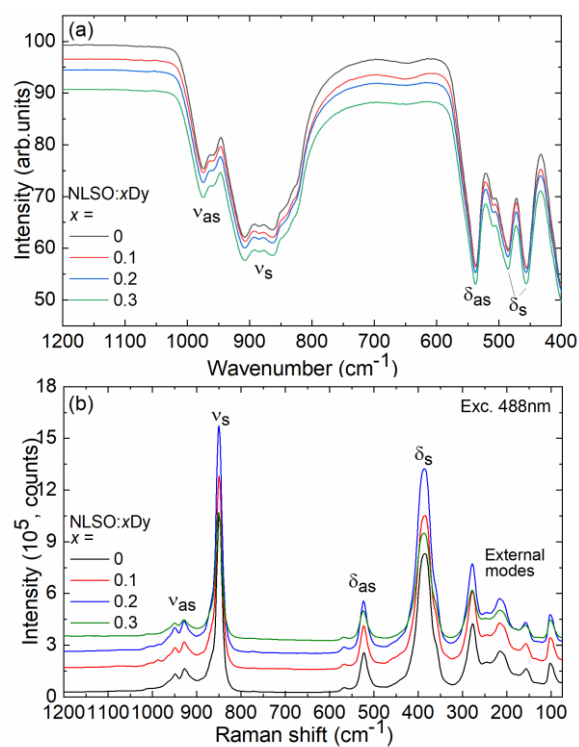


Fig. 4. RT IR (a) and Raman (b) spectra of NLSO:xDy ($x = 0, 0.1, 0.2$ and 0.3) apatites. In (b), $\lambda_{\text{exc}} = 488$ nm.

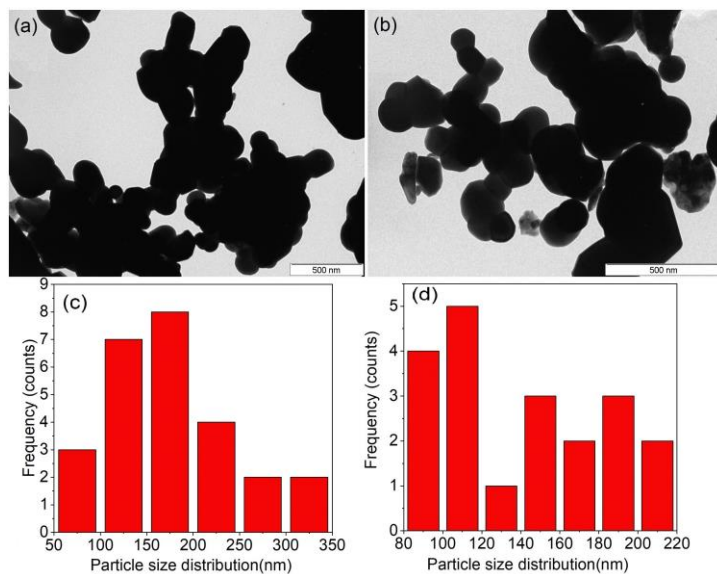


Fig. 5. (a,b) Typical TEM images and (c,d) the corresponding particle size distributions for (a,c) undoped NLSO and (b,d) NLSO:0.1Dy phosphors.

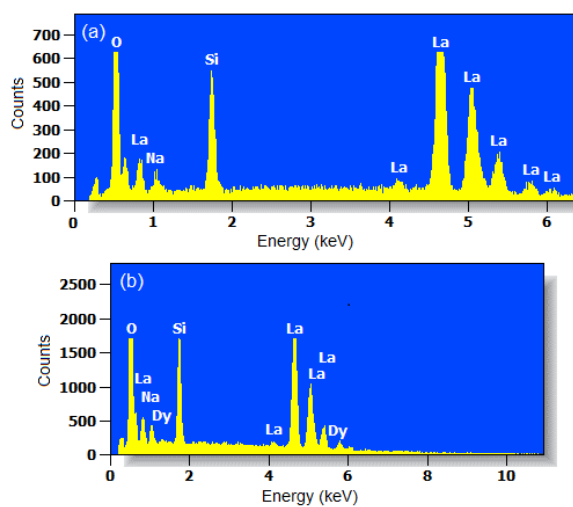


Fig. 6. Energy-dispersive X-ray (EDX) spectra of (a) undoped NLSO and (b) NLSO:0.1Dy samples.

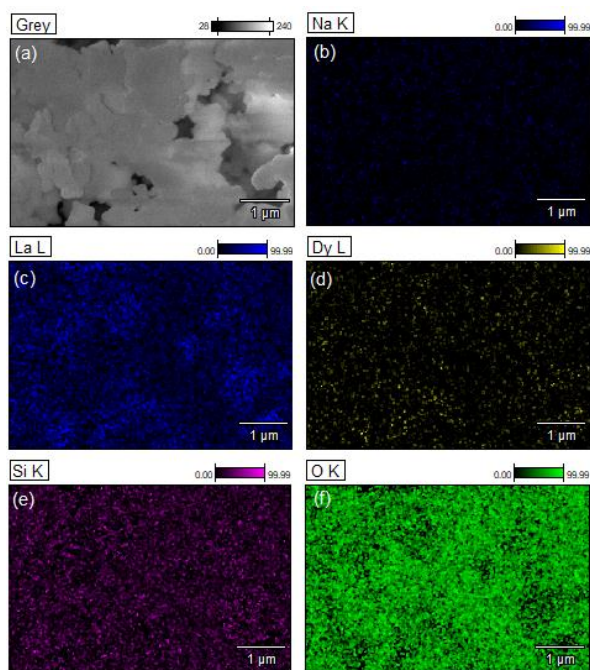


Fig. 7. Energy-dispersive X-ray (EDX) element mapping for the NLSO:0.1Dy sample: (a) SEM image; (b) Na (K-line); (c) La (L-lines); (d) Dy (L-lines); (e) Si (K-line); (f) O (K-line).

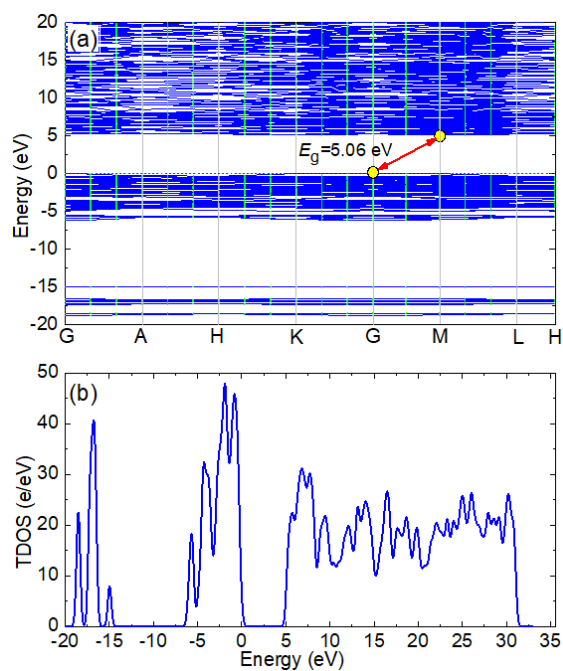


Fig. 8. Electronic structure of $\text{NaLa}_9(\text{SiO}_4)\text{O}_2$: (a) calculated band gap structure; (b) total density of states (TDOS).

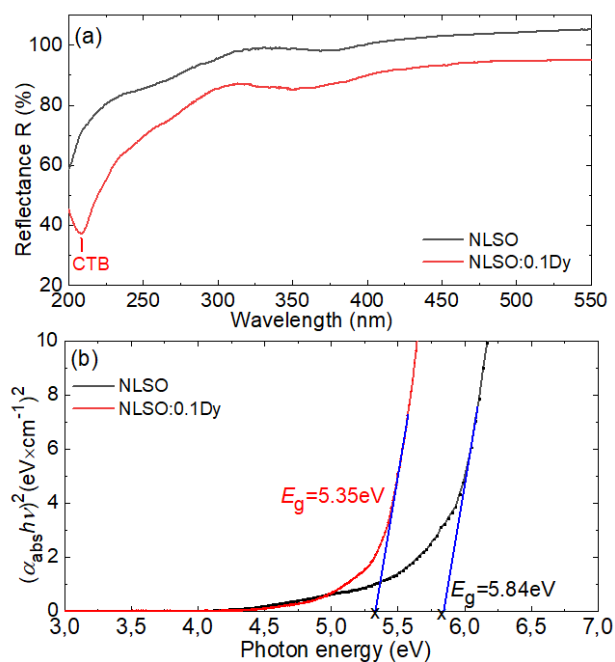


Fig. 9. (a) Diffuse reflectance spectra of undoped NLSO and NLSO:0.1Dy phosphors, CTB – charge transfer band; (b) the corresponding Tauc plots for the determination of optical bandgaps E_g (assuming indirect transitions).

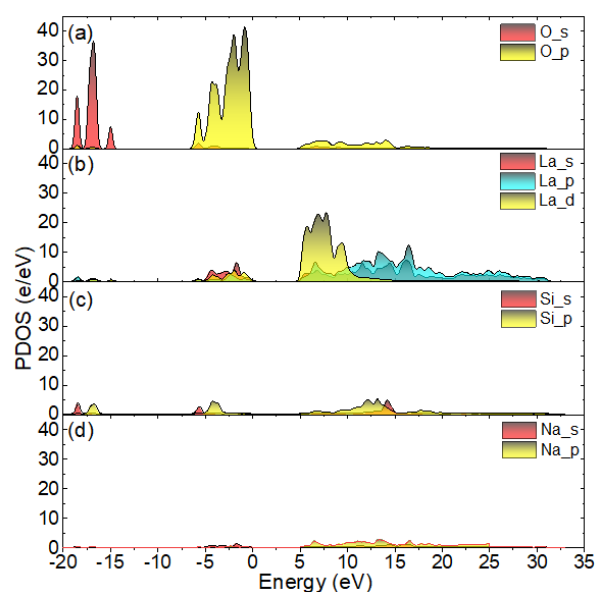


Fig. 10. Partial densities of states (PDOS) in NLSO: (a) O PDOS; (b) La PDOS; (c) Si PDOS; (d) Na PDOS.

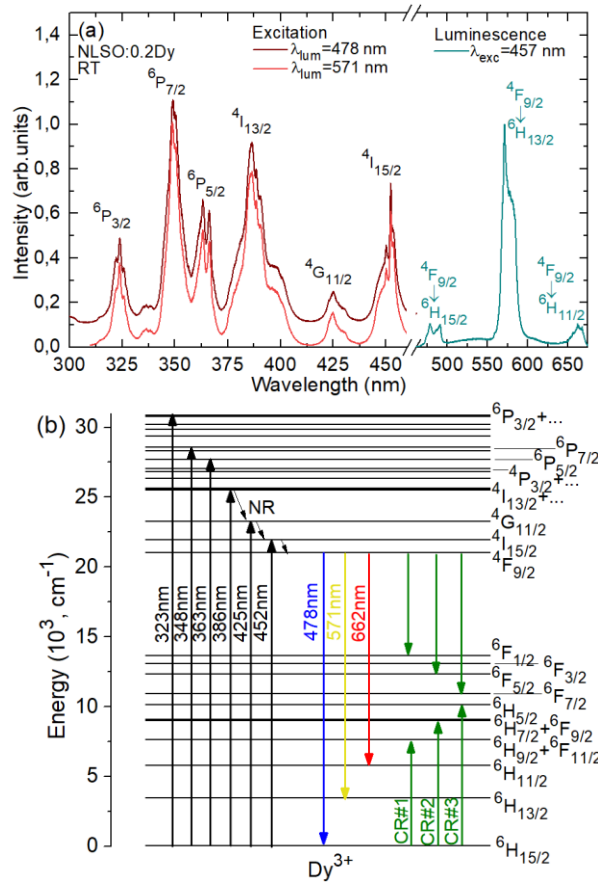


Fig. 11. (a) Photoluminescence excitation spectra of the NLSO:0.2Dy³⁺ phosphor for $\lambda_{lum} = 478$ nm and 571 nm; the luminescence spectrum for $\lambda_{exc} = 457$ nm is shown for comparison; (b) The scheme of energy-levels of Dy³⁺ ions showing transitions in absorption and emission, NR – multiphonon non-radiative relaxation, CR – cross-relaxation.

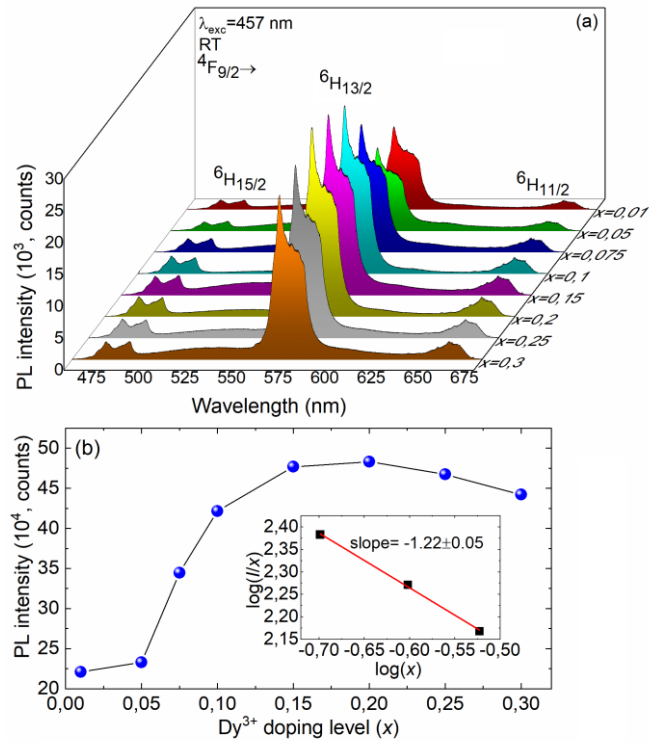


Fig. 12. (a) RT photoluminescence (PL) spectra of NLSO:xDy phosphors with different Dy³⁺ doping levels, $\lambda_{exc} = 457$ nm; (b) the variation of the integral intensity of the ${}^4F_{9/2} \rightarrow {}^6H_{13/2}$ emission band versus the Dy³⁺ doping level, the *inset* shows the analysis of the interaction type using Dexter's equation.

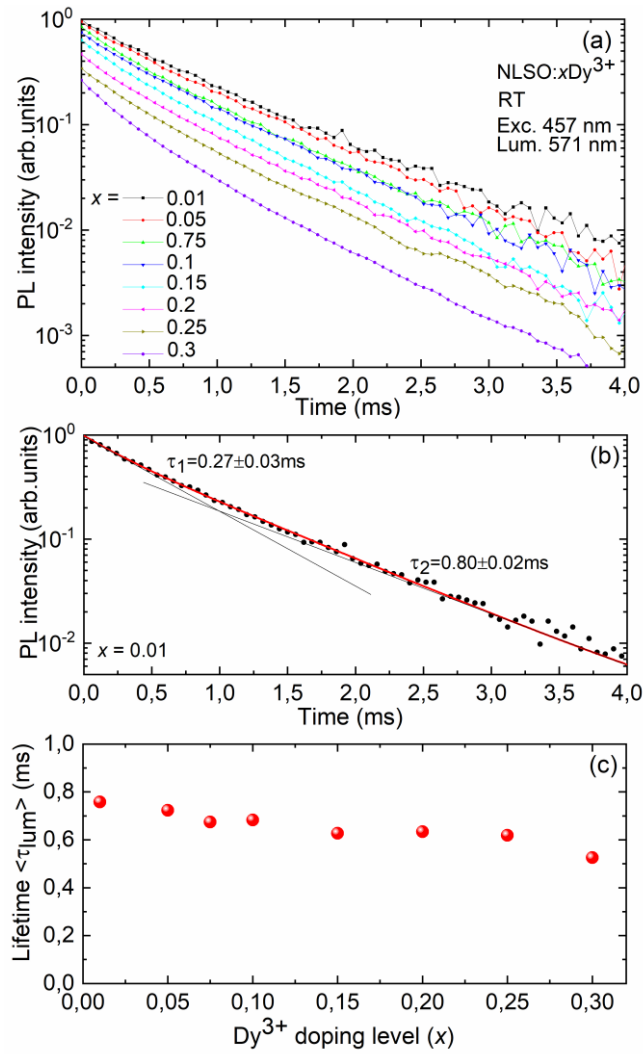


Fig. 13. (a) RT luminescence decay curves for NSLO: $x\text{Dy}$ phosphors, $\lambda_{\text{exc}} = 457 \text{ nm}$, $\lambda_{\text{lum}} = 571 \text{ nm}$; (b) biexponential fit of the decay curve for the sample with $x = 0.01$; (c) mean luminescence decay time $\langle \tau_{\text{lum}} \rangle$ as a function of Dy^{3+} doping level.

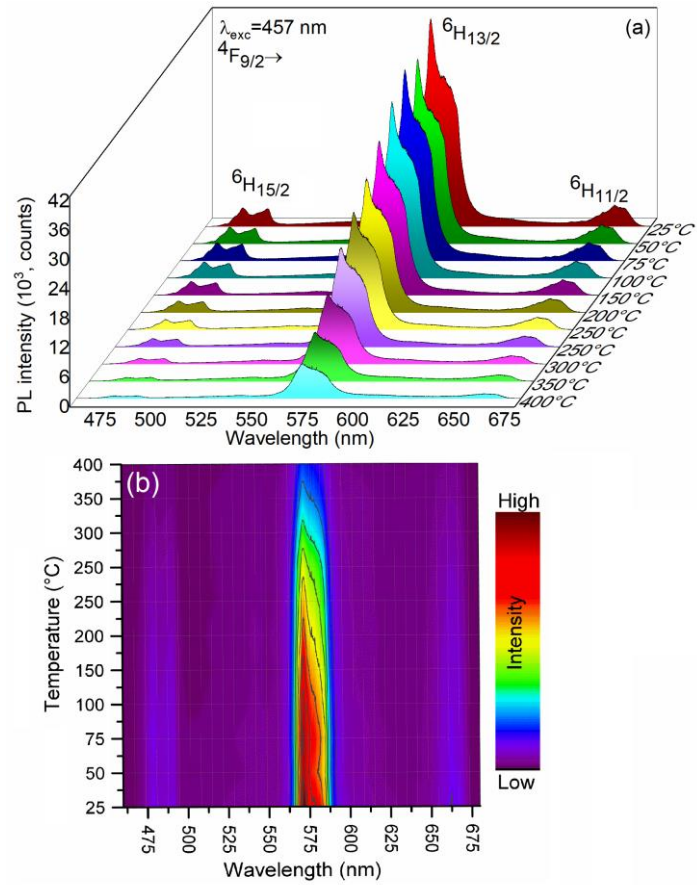


Fig. 14. (a) Temperature-dependent luminescence spectra of the NLSO:0.2Dy sample, $\lambda_{\text{exc}} = 457 \text{ nm}$; (b) the corresponding contour map.

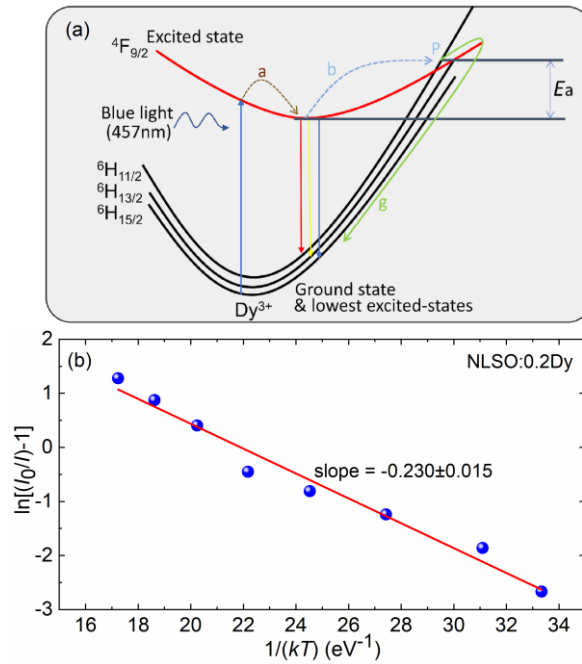


Fig. 15. (a) The configurational coordinate diagram for Dy^{3+} ions in NLSO; (b) evaluation of the activation energy for the NLSO:0.2Dy phosphor using an Arrhenius-type activation model, Eq. (5).

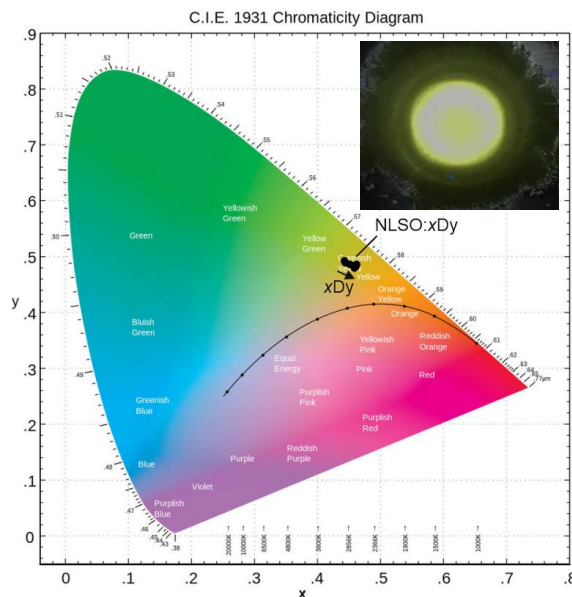


Fig. 16. The CIE 1931 chromaticity diagram showing the color coordinates for NLSO: x Dy phosphors, inset – photograph of the NLSO:0.15Dy sample under blue illumination.

Table 1. Crystallographic data and structure refinement parameters of undoped NLSO and NLSO:0.1Dy apatites.

Sample	NLSO	NLSO:0.1Dy
Chemical formula	NaLa ₉ (SiO ₄) ₆ O ₂	NaLa _{8.9} Dy _{0.1} (SiO ₄) ₆ O ₂
Crystal class		Hexagonal
Space group		<i>P6₃/m</i>
Number of formula units (Z)		1
Point group		<i>6/m</i>
General multiplicity		12
Reduced Number of S.O.		6
Calculated density (g/cm ³)	5.279	5.289
Lattice constants <i>a</i> = <i>b</i> , <i>c</i> (Å)	9.6917(3), 7.1836(4)	9.6897(5), 7.1825(4)
$\alpha = \beta, \gamma$ (deg.)		90, 120
Unit-cell volume <i>V</i> (Å ³)	584.357	584.018
2 θ range (deg.)		20 - 70
2 θ step (deg.)		0.02
Radiation		Cu K α 1 (λ = 1.54056 Å)
No. of reflections		192
Refinement software		Match3! software
Reliability factors	$R_p = 9.89, R_{exp} = 9.43,$ $R_{Bragg} = 2.56, R_{wp} = 13.8,$ $\chi^2 = 2.14$	$R_p = 10.0, R_{exp} = 9.43,$ $R_{Bragg} = 2.81, R_{wp} = 13.8,$ $\chi^2 = 2.15$

Table 2. Fractional atomic coordinates, occupancy factors (O.F.) and isotropic thermal factors (B_{iso}) of NLSO and NLSO:0.1Dy

Atoms	Wyckoff	<i>x/a</i>	<i>y/b</i>	<i>z/c</i>	O.F.	$B_{iso}, \text{Å}^2$
NLSO						
La1 Na	4 <i>f</i>	0.3333(3)	0.6667(0)	-0.0028(0)	0.750 0.250	0.65
La2	6 <i>h</i>	0.2316(1)	-0.0142(5)	1/4	1.00	0.89
Si	6 <i>h</i>	0.4026(0)	0.3707(1)	1/4	1.00	1.12
O1	6 <i>h</i>	0.3280(4)	0.4815(6)	1/4	1.00	0.98
O2	6 <i>h</i>	0.5880(5)	0.4631(0)	1/4	1.00	1.23
O3	12 <i>i</i>	0.3362(6)	0.2525(3)	0.0744(5)	1.00	1.08
O4	2 <i>a</i>	0	0	1/4	1.00	1.25
NLSO:0.1Dy						
La1 Na Dy1	4 <i>f</i>	0.3333(5)	0.6667(0)	-0.0031(2)	0.741 0.01 0.250	0.84
La2 Dy2	6 <i>h</i>	0.2215(3)	-0.0116(0)	1/4	0.999 0.011	1.03
Si	6 <i>h</i>	0.3926(3)	0.3453(9)	1/4	1.00	1.07
O1	6 <i>h</i>	0.3358(1)	0.4823(3)	1/4	1.00	1.27
O2	6 <i>h</i>	0.5866(3)	0.4756(2)	1/4	1.00	1.65
O3	12 <i>i</i>	0.3863(7)	0.2685(0)	0.0883(5)	1.00	1.02
O4	2 <i>a</i>	0	0	1/4	1.00	1.12

Table 3 Unit-cell parameters, unit-cell volume and Scherrer crystallite sizes of NLSO:xDy ($x = 0, 0.1, 0.2$ and 0.3).

xDy	0	0.1	0.2	0.3
a, b (Å)	9.6917(3)	9.6897(5)	9.6835(4)	9.6651(1)
c (Å)	7.1836(4)	7.1825(4)	7.1741(0)	7.1693(3)
V (Å ³)	584.357	584.018	582.589	580.377
$D_{(211)}$ (nm)	132	129	125	113

Table 4. Color coordinates (x, y) and correlated color temperatures (CCT) for NLSO:xDy phosphors.

xDy	x	y	CCT, K
0.01	0.452	0.501	3398
0.05	0.451	0.505	3432
0.075	0.459	0.498	3289
0.1	0.466	0.492	3162
0.15	0.468	0.493	3152
0.2	0.469	0.495	3150
0.25	0.469	0.498	3157
0.3	0.470	0.498	3152

Table 5. A comparison of the emission properities of Dy³⁺-activated apatites phosphors.

Phosphor	x	y	color	CCT, K	τ_{lum} , ms	Ref.
NaLa ₉ (SiO ₄) ₆ O ₂ :Dy	0.469	0.495	yellow	3150	0.63	This work
Ca ₅ Y ₃ Na ₂ (PO ₄) ₅ (SiO ₄)F ₂ :Dy	0.396	0.421	yellow	3916	--	[51]
Ca ₉ La(PO ₄) ₅ (SiO ₄)Cl ₂ :Dy	0.334	0.355	white	5436	0.53	[52]
Ba ₂ Y ₃ (SiO ₄) ₃ F:Dy	0.357	0.389	white	4738	1.07	[53]
La ₆ Ba ₄ (SiO ₄) ₆ F ₂ :Dy	0.342	0.378	white	5170	0.56	[54]
Ca ₉ La(PO ₄) ₅ (SiO ₄)F ₂ :Dy	0.356	0.366	white	4663	0.57	[55]